Heterogeneity of Scaling of the Observed Global Temperature Data

SUZANA BLESIĆ, DAVIDE ZANCHETTIN, AND ANGELO RUBINO

Department of Environmental Sciences, Informatics and Statistics, Ca'Foscari University of Venice, Mestre-Venice, Italy

(Manuscript received 5 December 2017, in final form 1 November 2018)

ABSTRACT

We investigated the scaling properties of two datasets of the observed near-surface global temperature data anomalies: the Met Office and the University of East Anglia Climatic Research Unit HadCRUT4 dataset and the NASA GISS Land–Ocean Temperature Index (LOTI) dataset. We used detrended fluctuation analysis of second-order (DFA2) and wavelet-based spectral (WTS) analysis to investigate and quantify the global pattern of scaling in two datasets and to better understand cyclic behavior as a possible underlying cause of the observed forms of scaling. We found that, excluding polar and parts of subpolar regions because of their substantial data inhomogeneity, the global temperature pattern is long-range autocorrelated. Our results show a remarkable heterogeneity in the long-range dynamics of the global temperature anomalies in both datasets. This finding is in agreement with previous studies. We additionally studied the DFA2 and the WTS behavior of the local station temperature anomalies and satellite-based temperature estimates and found that the observed diversity of global scaling can be attributed both to the intrinsic variability of data and to the methodology-induced variations that arise from deriving the global temperature gridded data from the original local sources. Finally, we found differences in global temperature scaling patterns of the two datasets and showed instances where spurious scaling is introduced in the global datasets through a spatial infilling procedure or the optimization of integrated satellite records.

1. Introduction

Global near-surface air temperature databases are standardly derived from long-term instrumental temperature measurements and are offered for public use to document and help understand historical and ongoing climate variations and change (Karl et al. 1993). The three most prominent groups that produce such databases are the NASA Goddard Institute for Space Studies (GISS), the NOAA/National Centers for Environmental Information [NCEI; formerly the National Climatic Data Center (NCDC)], and a joint effort of the Met Office Hadley Centre and the University of East Anglia Climatic Research Unit (with the corresponding dataset HadCRUT; Hansen et al. 2010; Morice et al. 2012; Smith et al. 2008). Input observations to these datasets are largely drawn from the same sources: the World Meteorological Organization (WMO) and Global Climate Observation System (GCOS) initiatives provide the bulk of the land station data (Morice et al. 2012; Jones et al. 2012), while the International Comprehensive Ocean–Atmosphere Dataset (ICOADS), a compilation of meteorological records collected by ships and drifting and tethered buoys, is the main source of the ground ocean data (Morice et al. 2012; Freeman et al. 2017). All the observational data are typically updated monthly (Morice et al. 2012). Despite their common sources of observational data, the datasets largely differ in how they handle issues such as incomplete spatial and temporal coverage or nonclimatic influences on a measurement station's environment (Hansen et al. 2010; Morice et al. 2012). Further, methodological differences in the construction of datasets include usage or lack thereof of spatial infilling (Hansen et al. 2010), incorporation of satellite measurements (Reynolds et al. 2002), and estimation of near-surface air temperature above sea ice (Smith et al. 2008; Hansen et al. 2010). Finally, all prominent global temperature datasets are given in the form of temperature anomalies, calculated against different climatological reference

Supplemental information related to this paper is available at the Journals Online website: https://doi.org/10.1175/JCLI-D-17-0823.s1.

Corresponding author: Suzana Blesić, suzana.blesic@unive.it

DOI: 10.1175/JCLI-D-17-0823.1

periods, with different resolutions of spatial averaging and interpolation (i.e., with different sizes of corresponding grid elements; Hansen et al. 2010; Morice et al. 2012; Smith et al. 2008).

Comparative assessments of these datasets indicate their consistency regarding certain components of temperature variability, such as hemispheric or global trends (Hansen et al. 2010). However, a reliable quantification of consistency lacks the estimation of uncertainty in the long-range spatial and temporal temperature characteristics, originated by both intrinsic variability of data and the structural differences between the datasets. In this regard, scaling properties are known to characterize correlated randomness (Stanley 2005) that persists over a wide range of time scales. In this paper, we investigate scaling properties of the two main global temperature datasets: the current versions of the HadCRUT (HadCRUT4) and NASA GISS Land–Ocean Temperature Index (LOTI). By calculating power-law exponents of appropriately prepared statistical functions that describe the gridded monthly data time series, we determine the existence and forms of global patterns of the observed near-surface air temperature stochastic variability and assess the influence of structural uncertainties that arise from the choice of a particular dataset preparation methodology on the quantification of the long-range spatial and temporal order of the data.

The role of stochasticity in climate state and variability has been extensively studied since the initial application of present-day scaling techniques in statistical hydrology (Hurst 1951; Mandelbrot 2001). Specifically, it was determined that observational and derived regional and global temperature data show strong natural long-term persistence. It can be described by the autocorrelation function $C(s)$ that decays by a power law of the separation time lag s (Tamazian et al. 2015; Carvalho et al. 2007; Tsonis et al. 1999, 2003) in such a way that the mean correlation time for infinitely long records diverges (a criterion for a long-term persistence, a long-range order, or a long-range memory). In this paper, we presume scaling to be a sign of the existence of such a long-range (correlated) order in data; for a critical discussion of this approach and alternative explanations, we refer to studies referenced by Kantelhardt et al. (2006). The existence of spatial heterogeneity in temperature long-range behavior was reported in systematic studies of persistence and trends in land station records (e.g., Bunde and Havlin 2002; Eichner et al. 2003; Govindan et al. 2003; Alvarez-Ramirez et al. 2008a; Ludescher et al. 2016) and, to a certain extent, in previous versions of the HadCRUT (i.e., HadCRUT2) gridded data as well (see Fraedrich and Blender 2003; Bunde et al. 2004; Fraedrich and Blender 2004). We aim to add to this body of knowledge by extending scaling analysis to consider the global average temperatures and the corresponding spatially resolved gridded data, in order to calculate complete gridded patterns of global temperature scaling for the two prominent datasets and their corresponding spatially resolved data. The implications of scaling in global temperature data encompass the choice of the appropriate null hypothesis for the statistical characterization of natural variability in detection and attribution studies (Koutsoyiannis 2003; Zorita et al. 2008; Lennartz and Bunde 2009, 2011; Markonis and Koutsoyiannis 2013; Varotsos et al. 2014; Tamazian et al. 2015; Ludescher et al. 2017) and the design of reliable statistical climate model alternatives (Ashkenazy et al. 2003; Tsonis and Roebber 2004; Berezin et al. 2012; Franzke et al. 2015), along with a contribution to understanding the complexity of temperature records' fluctuations (Mandelbrot and Wallis 1968; Stanley 2000).

In this paper, scaling properties of global temperature data are described through the scaling (or Hurst) exponent α of each temperature gridpoint time series. To determine α, we used second-order detrended fluctuation analysis (DFA2; see, e.g., Kantelhardt et al. 2001), where linear trends in the data are systematically removed. We used DFA2 in combination with the wavelet transform (WT) power spectral analysis to confirm the DFA2 results by determining the scaling exponent β of the wavelet power spectra (Blesić et al. 2003; Bashan et al. 2008). In addition, we used the wavelet transform power spectrum (WTS) to provide insight into the existence, positions, and amplitudes of significant periodic or nonperiodic cycles in the data (Sarvan et al. 2017; Stratimirović et al. 2018). To this end, we used Morlet wavelets of the sixth order as a wavelet basis for our analysis. The Morlet wavelets have been proven to possess the optimal joint time–frequency localization (Goupillaud et al. 1984; Torrence and Compo 1998) and can thus be effectively used to detect locations and spatial distribution of singularities in time series (Mallat and Hwang 1992; Zanchettin et al. 2008). We calculated the scaling exponents α for all the available gridpoint data of the two datasets, without restrictions regarding the amount of missing data. The purposes of this approach were to obtain global spatial pattern(s) of scaling, to examine its differences and similarities for two databases, to identify dissimilarities that stem from inhomogeneities due to data management (Karl et al. 1993; Peterson et al. 1998; von Storch et al. 2012), and to test the robustness of our methods against data nonuniformity (Hu et al. 2001; Chen et al. 2002; Rust et al. 2008). Our results may be compared with other methods

of data analysis, such as the Fourier transform power spectral analysis or the calculation of the autocorrelation function, through direct dependence (Talkner and Weber 2000; Höll and Kantz 2015) and scaling relations given below. Finally, our approach did not hypothesize any particular underlying physical process as a source of scaling. It can nevertheless be compared to the outputs of approaches based on other functional forms and/or specific model assumptions, such as with the structure functions analysis based on the concept of scale invariance in turbulence (Schertzer and Lovejoy 1987, 1990; Talkner and Weber 2000; Lovejoy and Schertzer 2013); for the comprehensive assessment of links of structure function analysis to DFA, please see Talkner and Weber (2000) and Kantelhardt et al. (2006).

Our paper is structured as follows. In section 2, we give a brief overview of the sources of data and of the general methodological framework of the DFA and the WTS analysis. In section 3, we present the results of the usage of DFA2 and WTS to study scaling properties of the HadCRUT4 and NASA GISS LOTI datasets. This includes our findings that concern possible sources of the observed anti-autocorrelated (with scaling exponents $\alpha < 0.5$) and highly autocorrelated (with $\alpha > 1$) behavior in some of the HadCRUT4 grid cells and the results of the use of DFA2 and WTS to understand the observed differences in scaling between HadCRUT4 and NASA GISS LOTI. We end our paper with a list of conclusions and a few suggestions for future work in section 4.

2. Data and methods

a. Data

We used the NASA GISS LOTI gridded monthly temperature anomalies data available on the GISS Surface Temperature Analysis (GISTEMP) website (GISTEMP Team 2017). We used the LOTI data derived from the analysis that combines the Extended Reconstructed Sea Surface Temperature (ERSST) version 4 (Huang et al. 2015; Liu 2012; Huang et al. 2016) dataset with optimum interpolation (OI) of the satellite data and with 1200-km spatial smoothing for insufficient coverage (Hansen et al. 2010). In GISTEMP, the grid boxes are 2° latitude × 2° longitude. We also used the Met Office Hadley Centre observational gridded dataset HadCRUT4, which provides median temperature anomalies from the 100 ensemble members in each grid box (Morice et al. 2012), available on the Met Office website (Met Office Hadley Centre 2010). In HadCRUT4, the grid boxes are 5° latitude × 5° longitude. For parts of our analysis that compare results obtained within particular grid elements with those obtained using the source observational data of the same grid cell, we used land station data provided by Google Earth for the HadCRUT4 land temperature dataset CRUTEM4 (Jones et al. 2012; Osborn and Jones 2014; CRUTEM4 Team 2017) and the NCDC Global Historical Climatology Network (GHCN; version 3) land station monthly data (Lawrimore et al. 2011; GHCN Team 2017). To compare our results for the gridded data with marine observations, we considered the ICOADS version 2.5 time series provided by the Royal Netherlands Meteorological Institute (KNMI) Climate Explorer web application (KNMI Team 2017). Whenever possible, we used both unadjusted and adjusted land station or marine measurements to account for the effects of data homogenization (Rust et al. 2008). Finally, as a source of satellite temperature measurements, we used the University of Alabama in Huntsville (UAH) satellite temperature analysis (Christy et al. 2003; Christy and Spencer 2017) in combination with the NCEI OI sea surface temperature (OISST; Banzon et al. 2016; Reynolds et al. 2007; OISST Team 2017); in UAH, the grid boxes are 2.5° latitude × 2.5° longitude, while the OISST dataset has a resolution of 1° latitude × 1° longitude. An overview of our data sources is given in Table 1.

Whenever the time series were given in absolute temperatures, and in order to correctly compare their DFA2 and WTS results with the corresponding outputs of HadCRUT4 and NASA GISS LOTI time series, we used conventional deseasoning to define their anomaly time series. In these instances, the seasonal means for the entire record, instead of for the particular reference period, have been removed (Livina et al. 2011; Torrence and Compo 1998). In this paper, we refer to such deseasoned records as the "raw data." This method of seasonal detrending has been proven appropriate for the purpose and design of our study [i.e., the assessment of (monofractal) scaling and consistency of cycles in data; Livina et al. 2011; Ludescher et al. 2011; Bunde et al. 2013a]; it dampens the amplitude of the annual cycle in the amount sufficient to enable the assessment of underlying long-term correlation properties. If the original absolute temperature date were used, this would lead to a remarkable change in DFA2 results; in the range of scales of interest to this paper, the seasonal trend will dominate DFA2 (and WTS) behavior in such a profound way that the estimation of scaling will be impossible, and DFA2 functions will be almost indistinguishable for different observational records (Hu et al. 2001).

b. Methodology

We used the DFA and the WTS approaches for data analysis. DFA was introduced as an appropriate scaling

TABLE 1. Monthly data sources with major parameters and number of data points N used for scaling analysis.

Source and version	Spatial resolution	Anomalies calculation and spatial infilling, not including the treatment of sea ice	Start year	N
HadCRUT4	5° × 5°	Average of observational data, with correction for errors as median of 100 realizations, weighted for all the nonmissing grid boxes in each hemisphere and averaged over hemispheres	1850	1820
CRUTEM4	5° × 5°	Average of observational data, with correction for errors, weighted in the same manner as HadCRUT4	1850	Various
GISS (GISTEMP) LOTI	2° × 2°	Average of observational data, with adjustment for errors and the addition of weighted averages of station records in the radius of 1200 km (alternatively, 250 km) from the gridcell center, weighted over zones by the zone's full area	1880	1640
GHCNv3	—	Unadjusted and adjusted (for nonclimatic influences) land station data	1701	Various
ICOADSv2.5	—	Quality controlled individual marine observations	1662	Various
OISSTv2	1° × 1°	OI of sea surface and satellite records	1981	420
UAHv6 (TLT)	2.5° × 2.5°	Quadratic approximation to the average control radiosonde data, with removed nonclimatic influences and intersatellite differences	1979	456

analysis to deal with nonstationary records that contain some trends of unknown form (Peng et al. 1994). In DFA, the procedure of detrending was devised so as to eliminate such trends. The resulting remarkable performance of this method in data analysis critically stems from this highly effective detrending solution, as shown by numerous systematic studies that investigate the effects of trends, nonstationarities, and nonlinearities (Hu et al. 2001; Chen et al. 2002, 2005), as well as the effects of extreme data loss (Ma et al. 2010) on the DFA function form, and compare DFA with other detrending methods (Xu et al. 2005; Bashan et al. 2008) or other independent methods of data analysis (Alvarez-Ramirez et al. 2008b; Rodriguez et al. 2014). Recently, a new mathematical insight further illuminated how DFA operates on nonstationary data series with nonstationarity due to their intrinsic dynamics (Höll et al. 2016).

We applied the version of DFA (Peng et al. 1994) that utilizes the detrending procedure on a set of overlapping segments (Buldyrev et al. 1995) of a time series of duration (number of data points) N, which is described in detail in Blesić et al. (1999) and Milošević et al. (2002). In this version of DFA, any time series $A(k)$ ($k = 1, \ldots, N$) is first transformed into a series of its partial (or cumulative) sums $y(l) = \sum_{k=1}^{l}[A(k) - A_{\text{ave}}]$, where $A_{\text{ave}} = (1/N)\sum_{k=1}^{N}A(k)$. For any given overlapping segment of length n of $y(l)$, $y_{n,i}(l)$ ($i = 1, \ldots, N - n + 1$), the procedure of detrending is applied: the local trend is calculated through a polynomial least squares fit (Kantelhardt et al. 2001) and subtracted from $y_{n,i}(l)$. The polynomial degree that defines the local trend represents the DFA order; in our case, it is two (i.e., we used a quadratic function). Finally, the average of variances about the local trend obtained over all segments is calculated (Peng et al. 1994), thereby producing the detrended fluctuation function:

$$F(n) = \sqrt{\frac{1}{(N-n+1)l}\sum_{i=1}^{N-n+1}\sum_{l=1}^{n}[y_{n,i}(l)]^2}. \qquad (1)$$

The function $F(n)$ increases with the segment length n (Blesić et al. 1999). If (any) $A(k)$ is short-range autocorrelated or has no correlations at all, $F(n)$ behaves as $n^{1/2}$ (Peng et al. 1994). For data with power-law long-range autocorrelations, the expectation is that $F(n) \sim n^{\alpha}$, with $\alpha \neq 0.5$. We call the data long-range autocorrelated, or long-term persistent (LTP), when the corresponding autocorrelation function $C(s)$ decays by a power law $C(s) \sim s^{-\gamma}$ for $s > 0$ and $N \to \infty$. If this is the case, γ represents the correlation exponent that quantifies the nature and the level of autocorrelations in the record; for stationary cases, γ lies in the range $0 < \gamma < 1$. Correlations are generally termed long-range when the mean correlation time, defined as $T = \int_0^{\infty} C(t)dt$, diverges (Höll and Kantz 2015) and thus cannot be used to define the characteristic time scale of autocorrelations. It can also be shown that in this case the Fourier power spectral density decreases as a power law as well, with $E_F(\omega) \sim \omega^{-\beta}$ and the exponent β in the range $-1 < \beta < 1$ (Peng et al. 1993). The exponent α, associated with the detrended fluctuation function $F(n)$, can be related to both γ and β through

scaling relations $\alpha = 1 - \gamma/2$ and $\alpha = (\beta + 1)/2$ (Peng et al. 1993). This bounds α to a range $0 < \alpha < 1$ for stationary records, where $0.5 < \alpha < 1$ indicates persistence in the record. Instances when $\alpha \geq 1$ imply the existence of intrinsic nonstationarities in the autocorrelated data (Höll et al. 2016); in this case, DFA functions exhibit crossovers, while $\alpha \geq 1$ may mean that the underlying process is of a composite nature (Höll and Kantz 2015) or that there exists an imbalance between different noise inputs (Peng et al. 1995). Finally, $\alpha = 1.5$ indicates brown noise, the integration of white noise.

The advantages of using DFA over the more conventional statistical approaches (such as the calculation of the autocorrelation functions or the Fourier power spectra) for the analysis of records from complex systems are twofold, and both stem from the method design. First, DFA takes any typical time-dependent discrete data series—which is, in general, likely nonstationary and with unknown trends—and produces a series that fluctuates much less than the original by subtracting local trends at different time window lengths. The remaining time series has the same statistical properties as the original (Stanley 2000) but is now prepared in a way that greatly helps clarify its dynamic behavior. Second, direct calculations of the autocorrelation function, or of Fourier power spectra, are hindered by the level of noise present in a typical natural record by the possible nonstationarities in the data. DFA, however, calculates the fluctuation function, which is, by definition, a sum over autocorrelations (Höll and Kantz 2015), and thus fluctuates less. As a result, one uses a function that is entirely defined by the autocorrelation function but is more stable (Bunde et al. 2013b), allowing for clearer (or less noisy) presentation and interpretation of the results on (log–log) graphs. In the online supplemental material, we provide a graphical illustration of these claims for the statistical functions of the time series of HadCRUT4 global temperature anomalies.

Pure, long-range autocorrelated behavior rarely occurs in natural records. The corresponding DFA2 functions, depicted on the log–log graphs, are thus rarely ideal linear functions. Instead, they tend to display transient crossovers in scaling that stem from occurrences of irregular phenomena of different types (Mallat and Hwang 1992; Hu et al. 2001). Of those, climate records are likely to embed effects of mixtures of cyclic components that can cover a whole band of frequencies and locally perturb scaling (including DFA2) analysis (Mandelbrot and Wallis 1969). It has been shown (Hu et al. 2001) that these perturbations present in a form of peak-like structures, superposed on the DFA functions of a pure long-range correlated signal, with widths wider than those that would be expected from single sharp periodic waves. The spread of any such perturbation, and the length of scales that it covers until asymptotically resuming to the DFA behavior dominated by the long-range correlated noise, depends on the scaling exponent α and the period and/or amplitude of the hypothetical periodic trend and is generally much less visible for the greater values of α [see detailed explanations and theoretical relations by Mandelbrot and Wallis (1969) and Hu et al. (2001)]. When the effects of such irregularities are visible on DFA2 curves but are not comparatively strong to change the global behavior of DFA2 functions, we use WT analysis to investigate them.

The WT was introduced in order to circumvent the uncertainty principle problem in classical signal analysis (Stratimirović et al. 2018) and achieve better signal localization in both time and frequency than classical Fourier transform approaches (Morlet 1983; Grossmann and Morlet 1984). In WT, the size of an examination window (equivalent to the size of a sliding segment in DFA) is adjusted to the frequency analyzed. In this way, an adequate time resolution for high frequencies and a good frequency resolution for low frequencies is achieved in a single transform (Bračič and Stefanovska 1998).

The continuous WT of a discrete sequence $A(k)$, as defined by Morlet (1983) and Grossmann and Morlet (1984) and described in detail in Stratimirović et al. (2001) and Milošević et al. (2002), is the convolution of $A(k)$ with wavelet functions $\psi_{a,b}(k)$: $W(a, b) = \sum_{k=0}^{N-1} A(k)\psi^*_{a,b}(k)$. Here, a and b are the scale and translation-in-time (coordinate) parameters, and the asterisk stands for complex conjugate. To obtain the kind of results comparable with those of the DFA method, we calculated the wavelet scalegrams (mean wavelet power spectra) $E_W(a)$, which are defined as $E_W(a) = \int W^2(a, b)db$. The scalegram $E_W(a)$ can be related (Perrier et al. 1995) to the corresponding Fourier power spectrum $E_F(\omega)$ via the formula

$$E_W(a) = \int E_F(\omega)|\hat{\psi}(a\omega)|^2 \, d\omega, \tag{2}$$

where the hat designates the Fourier transform, while $E_F(\omega) = |\hat{A}(\omega)|^2$. It stems from Eq. (2) that if either of the two spectra—$E_W(a)$ or $E_F(\omega)$—exhibits power-law behavior, then the other will be of the power-law type as well, with the same power-law exponent β (Stratimirović et al. 2001). The meaning of the wavelet scalegram is the same as that of the classical Fourier spectrum: it calculates the contribution to the signal energy along the scale of a.

In this paper, we found it convenient to use the standard set of Morlet wavelet functions as a wavelet basis for our analysis (Morlet 1983; Grossmann and Morlet 1984). The Morlet wavelet, a plane wave modulated by a Gaussian, is a complex nonorthogonal wavelet function (Torrence and Compo 1998) that is recommended for use in time series analysis in instances where smooth, continuous variations in wavelet amplitude are expected (Torrence and Compo 1998). We choose to use the Morlet wavelet of order six, so as to also be able to utilize its shape for localization of singular time events (Bračič and Stefanovska 1998). It has been shown that that this wavelet transform is particularly well adapted to estimate the local regularity of functions (Mallat and Hwang 1992); namely, in the local wavelet power spectra, the Morlet wavelet is narrow in spectral (scale) space and broad in the time space, which produces very well-localized, relatively sharp peaks in the global WT spectra, the averages of local spectra over time (Torrence and Compo 1998). This choice provides us with a possibility to investigate effects of influence of both periodic and nonperiodic cycles on the dynamics of our data, together with the effects of occurrences of significant singular events (e.g., volcanic eruptions). Finally, by construction, the Morlet wavelet scale is almost equal to the Fourier scale (Torrence and Compo 1998), which makes the two power spectra comparable.

We calculated DFA2 fluctuation functions (DFA2ff) and WT power spectra (WTS) for the temperature anomalies data series and plotted them on double logarithmic time/scale axes so that the exponents α or β are estimated by linear fit. We took into consideration only the values of DFA2ff between the minimum time scale of $n = 5$ and the statistically meaningful maximum time scale of $n = N/5$ that we decided to use, following recommendations by Hu et al. (2001), Kantelhardt et al. (2001), Chen et al. (2002), Bashan et al. (2008), and Ludescher et al. (2017). Similarly, we calculated WTS between the time scales of $n = 1$ and $n = N/5$, following the argument that the upper meaningful time scale for the use of Morlet wavelets can be even higher than $N/5$ (Bračič and Stefanovska 1998). In searching for cycles in WTS, however, we looked for characteristic peaks (i.e., local maxima) just within the limits of maximum meaningful scale set at $n = N/10$ (Koscielny-Bunde et al. 2006). To ensure that the peaks that we obtained in such a way are not artifacts of the WT design, we additionally performed a test of statistical significance for each peak (Stratimirović et al. 2018), using the tool kit described by Torrence and Compo (1998) and ready-to-use software available on the University of Colorado Boulder's website (Torrence and Compo 2017). The significance of each peak was determined by comparing its amplitude against the background global wavelet spectrum for the corresponding time scale. This choice was guided by the consideration that the time series of temperature anomalies describe the evolution of a complex system that results from interactions of many constituents acting on different time scales (Liu 2012; Zanchettin 2017) and are thus mixtures of noise components from different inputs involved in the process (Stratimirović et al. 2018).

3. Results

We calculated the DFA2ff and the WTS and their corresponding scaling exponents α and β for the HadCRUT4 and NASA GISS LOTI global average time series of temperature anomalies, and the DFA2 exponents α for each gridpoint time series, for the two temperature anomaly products. In Fig. 1, we present the combined DFA2–WTS results for the global average HadCRUT4 and NASA GISS LOTI series, together with their raw data; here, and hereafter, DFA2–WTS represents the abbreviated notation for the results independently derived from DFA2 and WTS. In Fig. 1, the DFA2ff and the WTS are depicted in the form $F(n)$ versus n and $\sqrt{E_W(n) \times n}$ versus n, so as to provide a simple visual comparison of two methods, given the scaling relation $\alpha = (\beta + 1)/2$. For the HadCRUT4 global average series, we obtained $\alpha = 0.92 \pm 0.04$, while the NASA GISS LOTI time series yields $\alpha = 0.97 \pm 0.04$. Even if they leave the obtained scaling law valid, small deviations from the straight lines are already visible on both DFA2 plots presented. The use of WT enabled us to define these deviations as cycles and/or singularities present at the annual, two interannual, and near-decadal levels in HadCRUT4, and as the annual, interannual, and decadal variabilities in NASA GISS LOTI series. The calculated values of the scaling exponents α and β align for both data series within the range of the standard deviation of α that depends on the time series length N (Bashan et al. 2008), in agreement with previous findings (Markonis and Koutsoyiannis 2013; Lennartz and Bunde 2011). In what follows, we separately illustrate the results for the gridpoint time series for the two datasets, then explore their differences.

a. *Global pattern of scaling: HadCRUT4*

Figure 2 shows the global scaling pattern of the time series of HadCRUT4 gridded temperature anomalies. Depicted are values of the scaling exponent α for the time series of each grid point on the 5° × 5° grid, together with the latitudinal averages of the exponent α. Long-range correlated behavior is found in all of the

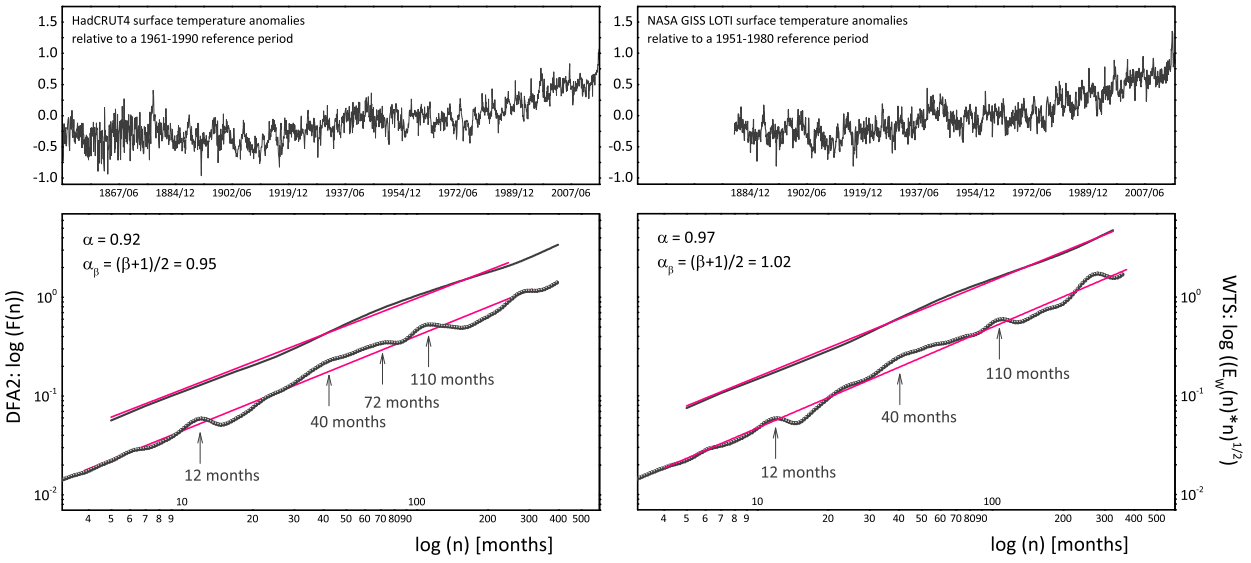

FIG. 1. Results of the DFA2–WTS analysis of the time series of global average temperature anomalies of the HadCRUT4 and NASA GISS LOTI datasets. (top) Data and (bottom) DFA2ff (solid lines) and WTS (filled circles) functions, together with linear fits to the DFA2ff and WTS curves (pink solid lines). The DFA2ff and the WTS are depicted on a log–log graph, in the form $F(n)$ vs n and $\sqrt{E_W(n)\times n}$ vs n, to allow for visual comparability between the two methods. Values of the DFA2 exponent α and the corresponding WTS exponent α_β are provided; for the estimation of errors to DFA2 exponents, see Bashan et al. (2008). Significant WTS peaks are marked with arrows.

grid points belonging to the ocean regions and in nearly all grid points on land (in 27 land grid cells, we found $0.45 \leq \alpha \leq 0.5$). There is a land–ocean contrast in persistence, with marine data that feature a substantially more pronounced LTP than land data, a result that agrees with previous findings based on individual station data (Bunde and Havlin 2002) and the partial assessment of the HadCRUT2 grid (Fraedrich and Blender 2003). Our results additionally reveal the nonuniformity of scaling within ocean as well as land data: this is how, for example, there is a region of higher-than-average LTP in the tropical land data, possibly following the distribution of rain forests; a region of lower-than-average LTP that differentiates the Indian Ocean from other basins (e.g., Zanchettin et al. 2013) that can be a signature of the South Equatorial Current (Rybski et al. 2008); or instances of higher-than-average LTP in various ocean basins that is arguably a signature of currents (in upwelling regions or at the Subpolar Gyre in the North Atlantic Ocean). At the basin scale, the spatial patterns of LTP values highlight differences in large-scale modes of sea surface temperature variability. For instance, the North Pacific and, especially, the North Atlantic Oceans display high persistence, whereas the tropical Indian Ocean displays weaker persistence. The former basins are expected to be dominated by modes of sea surface temperature variability at decadal and multidecadal time scales, namely, the Pacific decadal oscillation and the Atlantic multidecadal oscillation (e.g., Zanchettin et al. 2013), whereas the latter basin is dominated by interannual sea surface temperature variability (Zanchettin et al. 2013). Therefore, the global LTP pattern consistently relates with large-scale modes of climate variability, which provides a useful framework to interpret the physical meaning of the LTP values. To enable a detailed examination of the heterogeneity of HadCRUT4 global temperature scaling, we provide two additional maps of the global scaling pattern in the online supplemental material, with the interval thresholds of mapping set at ½ and ¼ of the interval presented in Fig. 2.

Figure 2 also shows latitudinal averages of the DFA2 exponent α, calculated along the 36 latitude rows of the HadCRUT4 dataset. It presents a weak latitude dependence of α, with lower LTP in high latitudes; this pattern seems to follow the global distribution of land and is probably somewhat affected by the strong influence of El Niño–Southern Oscillation (ENSO) teleconnections in the midlatitudes (Graf and Zanchettin 2012). The global averages of the scaling exponent α—the normal average, calculated as the average of all the DFA2 exponents of all the grid cells (when it is $\alpha_{\text{ave}}^{\text{hcn}} = 0.64 \pm 0.04$), and the weighted average, averaged according to the gridcell areas (with weights equal to the cosines of the central latitudes of each grid box (Met Office Hadley Centre 2010), which yields

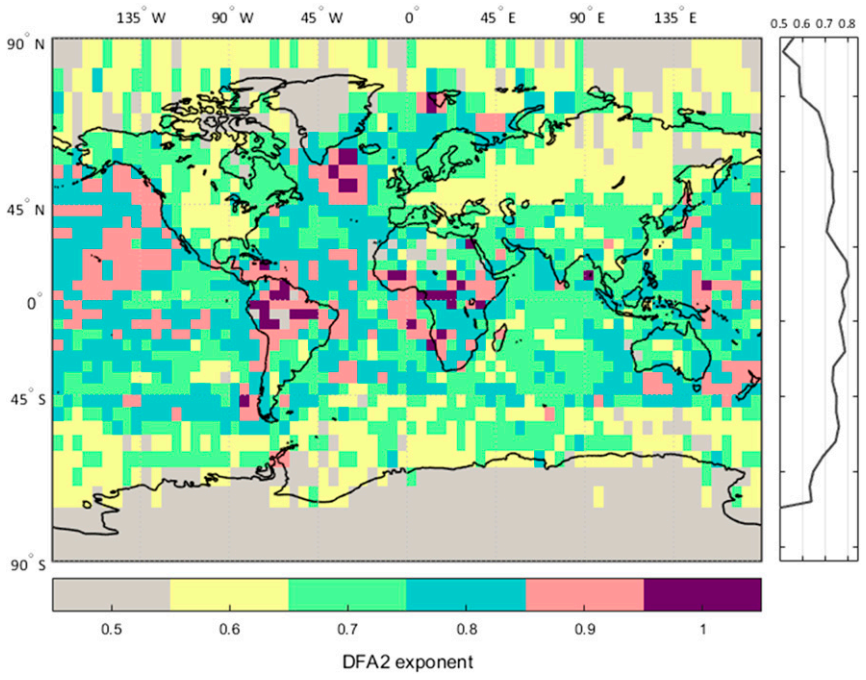

FIG. 2. (left) DFA2 exponents α calculated for all available gridpoint time series of temperature anomalies in the HadCRUT4 dataset. Values of $0 < \alpha < 0.45$ belong to grid boxes with missing data. (right) Latitudinal averages of α, calculated along the 36 latitude rows of the HadCRUT4 dataset (y-axis grid lines are inserted as visual guides).

$\alpha_{\text{ave}}^{\text{hcw}} = 0.72 \pm 0.04$)—are different from the value of α that we obtained for the global time series, $\alpha = 0.92 \pm 0.04$ (shown in Fig. 1). This result may be explained if we keep in mind the dataset construction methodology. Namely, the HadCRUT4 global temperature series (and similarly, NASA GISS LOTI; see Table 1) is constructed as the weighted average of all the nonmissing gridbox anomalies, which are themselves (nonweighted, except for the grid cells composed of a combination of land and marine data) spatial averages of instrumental records enclosed in each grid box. The process of averaging merges (adds) values of monthly data points from different records and thus superposes their different scaling and different cyclic amplitudes and distribution, producing a global temperature signal that wields the scaling properties of all the averaged data, together with the influence of all their cycles combined. The DFA2–WTS analysis of such a signal will naturally register all these influences. A similar combination of signals was studied in the systematic assessment of effects of nonstationarities on DFA by Chen et al. (2002), where different artificially generated time series with different scaling exponents α were used to analyze properties of signals comprising segments of these time series. The study reported that ''the behavior of $F(n)/n$ for a nonstationary signal comprised of mixed segments with different correlations is dominated by the segments exhibiting higher positive correlations even in the case when their relative fraction in the signal is small.'' At that time, the authors found this observation to be pertinent to real physiological records and to be true even in cases when signals of high positive correlations comprise only 10% of the entire time series. In the supplemental material, we assessed this dominance for the HadCRUT4 temperature data, in relation to the theoretical superposition rule provided by Chen et al. (2002), and found that the effect described by Chen et al. (2002) agrees well with the averages of individual gridcell or observational record DFA2 functions, but the dominance of the high LTP time series is even more pronounced in DFA2 functions of time series that were made as averages of individual gridcell or observational records first. In other words, even if signals with high LTP are not dominant by appearance in the global temperature pattern (which is evident from the values of $\alpha_{\text{ave}}^{\text{hcn}}$ and $\alpha_{\text{ave}}^{\text{hcw}}$), and even if they may not significantly affect the local scaling (the HadCRUT4 global scaling pattern is heterogeneous), they will have a significant relative influence on regional and global temperature scaling. Because both analysis products weight the temperature

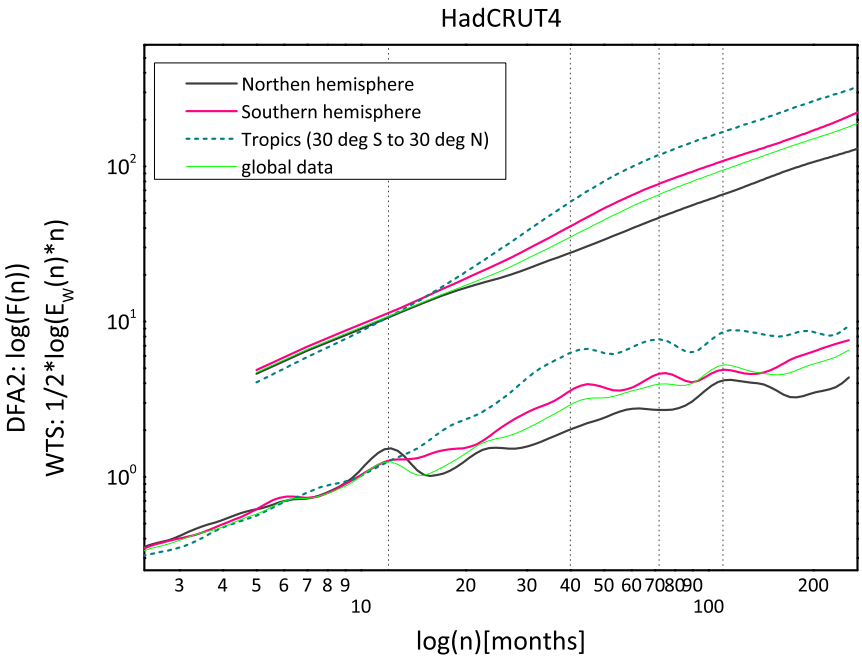

FIG. 3. Results of the DFA2–WTS analysis of the time series of global average temperature anomalies of the HadCRUT4, together with the average temperature anomalies for the Northern and Southern Hemispheres and the tropics, presented as in Fig. 1. Dotted vertical lines at t = 12, 40, 72, and 110 months are given as visual guides.

anomalies of grid cells by the cell's full area, this is probably especially true for the dominance exhibited by the high LTP of gridcell data along the midlatitudes. Figure 3 demonstrates this effect in the case of the DFA2–WTS functions for the HadCRUT4 averaged data for the Northern Hemisphere, Southern Hemisphere, and tropics. As shown in Fig. 3, the Southern Hemisphere has larger LTP than the Northern Hemisphere, mainly because the Southern Hemisphere holds a larger area of ocean and a smaller area of the land surface, and because of the ocean–land contrast in persistence. It is additionally obvious from Fig. 3 that global HadCRUT scaling follows (or is dominated by) the Southern Hemisphere scaling that is, in turn, likely largely influenced by the scaling at the tropics.

To understand how the obtained results are affected by the data loss in regions where large amounts of source data are missing, were removed due to artifacts in the observational records (Fraedrich and Blender 2003), or underwent a considerable adjustment due to inhomogeneous observations (Menne and Williams 2009; Alexandersson 1986), we compared the DFA2ff and WTS behavior of the raw (unadjusted) and the adjusted data for several such land stations. Because of the large amount of data, we could not investigate these effects for all records; we made a choice to focus our analysis on land stations that are the sole source or one of the few sources of observations available in the considered grid cell. Our results, shown in Fig. 4 for two illustrative examples, demonstrate that in such cases, the DFA2 exponents for the adjusted data in the gridded dataset can be slightly or even substantially smaller than for the raw data. The corresponding WTS reveals that this is probably due to the modulation of the annual cycle, as well as to the strong dampening of interannual and decadal fluctuations in the adjusted data. Artificial reduction of LTP by data adjustment seems to be a general feature. The opposite behavior (i.e., an increase of LTP by data adjustment, as shown in Fig. 5) only occurs in several polar or subpolar stations. There, systematic lack of data for entire seasons yields DFA2 exponents of the adjusted series that are slightly higher than those of the corresponding raw series, probably as a result of superposition of seasonality to the data. These findings indicate that the true DFA2 exponents for a largely predominant part of the HadCRUT4 grid, where there is a large percentage of missing values (Fraedrich and Blender 2003), are likely higher than those estimated from the actual gridded data and illustrated in Fig. 2. Our conclusion about a likely underestimation of the DFA2 exponent is in line with previous findings on effects of homogenization (Rust et al. 2008) on artificial data. The results also suggest that, excluding

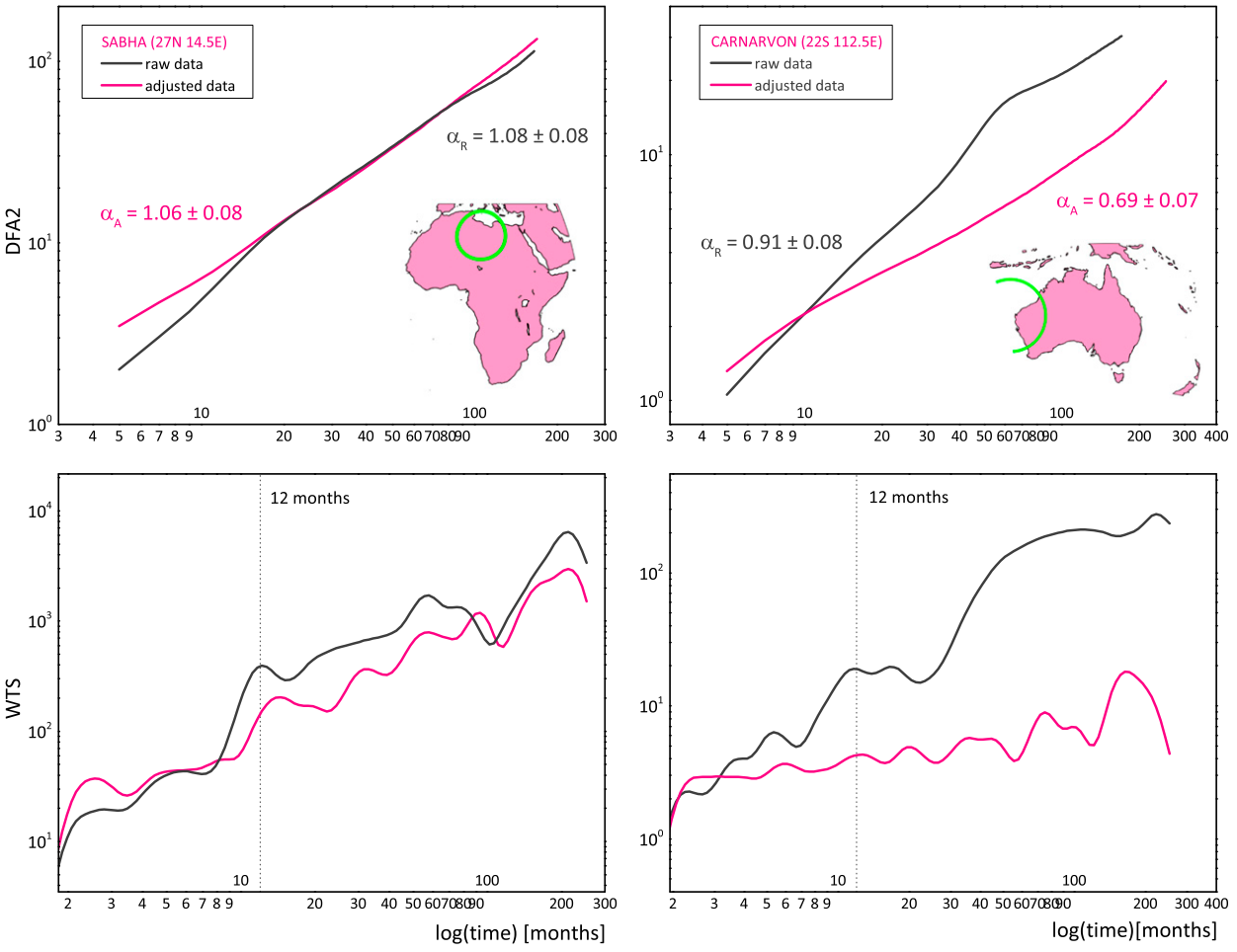

FIG. 4. Two examples of the (top) DFA2ff and (bottom) WTS calculated for the raw and adjusted temperature records of stations from the HadCRUT4 gridded dataset with (left) considerable amount of missing data and (right) observations that were preprocessed for data homogenization. In the DFA2ff graphs, the values of scaling exponents are given for both raw (unadjusted) data α_R and adjusted data α_A. In WTS graphs, dotted vertical lines at $t = 12$ months are given as visual guides. The coordinates indicating locations of land stations are given in the graph legends.

polar and parts of subpolar regions for substantial data inhomogeneity, the HadCRUT4 global temperature is long-range correlated (i.e., all the gridded DFA2 exponents are likely equal to or higher than 0.5).

Finally, we inspected the DFA2ff that have scaling exponent values larger than 1 to determine whether they display crossovers and thus the existence of intrinsic nonstationarities (Höll et al. 2016) that should then be explored and understood further. None of the HadCRUT4 grid points with $\alpha > 1$ has a crossover in DFA2 behavior. The comparison with corresponding WTS, provided in Fig. 6, shows that the DFA2–WTS slopes are this large probably owing to the strong interannual and multidecadal variability in their underlying data series that, in the time range of statistical significance of our results, may contribute to a slight overestimation of the scaling exponent α. This result seems to follow up on the existing research that investigates scaling of instrumental and proxy records of global temperature on much larger time scales. In particular, Lovejoy and Schertzer (2013) and Markonis and Koutsoyiannis (2013) indicate that probably no prominent source of nonstationarity exists that would change the scaling regime and produce crossovers in the scaling behavior in the range of the instrumental data that we are interested in (up to one decade). Because of the limited range of statistically meaningful scales for instrumental records, we were not able to further verify whether the scaling depicted in Fig. 6 is a part of the underlying very long-term persistent (Rybski et al. 2008; Markonis and Koutsoyiannis

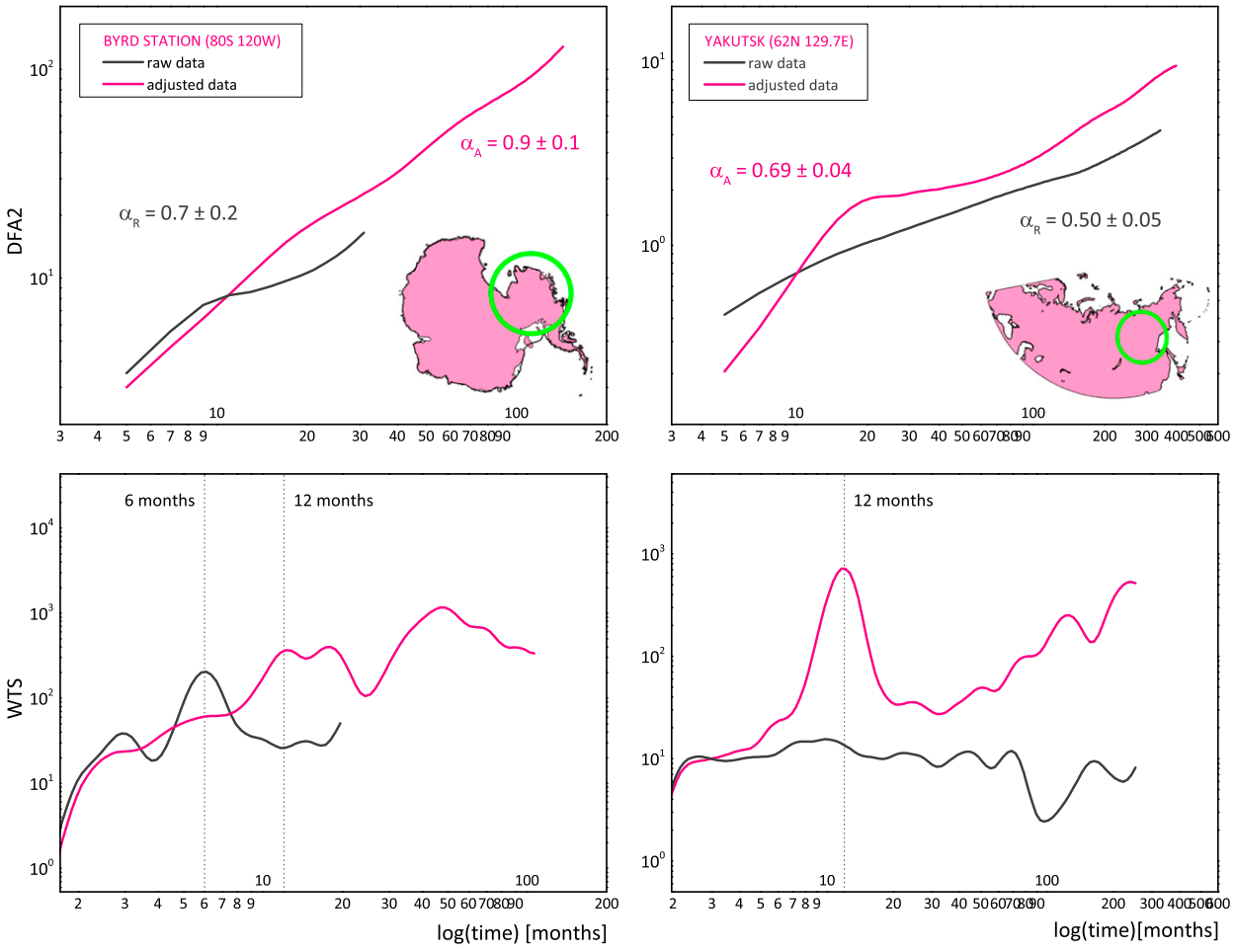

FIG. 5. Two examples of the (top) DFA2ff and (bottom) WTS calculated for the raw (unadjusted) and adjusted temperature HadCRUT4 records of (left) polar or (right) subpolar stations that systematically miss data for entire seasons. In the DFA2ff graphs, the values of scaling exponents are given for both raw data α_R and adjusted data α_A. In WTS graphs, dotted vertical lines at $t = 6$ and 12 months are given as visual guides. The coordinates indicating locations of land stations are given in the graph legends.

2013) or antipersistent (Carvalho et al. 2007; Lovejoy and Schertzer 2013; Luo et al. 2015) order.

b. *Global pattern of scaling: NASA GISS LOTI*

Figure 7 shows the DFA2 global pattern for the NASA GISS LOTI 2° × 2° gridded time series, together with latitudinal averages over 90 GISS latitudes, which produce the normal average over all grid cells of $\alpha_{\text{ave}}^{\text{gissn}} = 0.74 \pm 0.04$ and the weighted average of $\alpha_{\text{ave}}^{\text{gissw}} = 0.81 \pm 0.04$. Additional maps, created with lower-interval thresholds, are provided in the supplemental material. Visual comparison between Fig. 2 and Fig. 7 suggests that the NASA GISS LOTI and the HadCRUT4 data display a similar global pattern of scaling. There are, however, noticeable differences between both datasets: NASA GISS data display much more homogeneity in scaling within land and within ocean regions, with higher α values than HadCRUT4 over the ocean and lower α values over the land. An estimate of the distribution and the range of differences in values of α between the two datasets is given in Fig. S3 in the supplemental material. Over the ocean, particularly high values of the DFA2 exponent exceeding $\alpha = 1$ are identified in key regions of oceanic and coupled atmosphere–ocean variability, such as ENSO in the equatorial Pacific and at the sea ice edge south of Spitsbergen. In contrast with the HadCRUT4 dataset, where the Indian Ocean emerges as a peculiar oceanic region with low DFA2 exponents, the NASA GISS dataset yields high DFA2 exponent values, especially west of the Maritime Continent. These differences in persistence are linked to different representations of climatic modes in both datasets, particularly regarding those centered over the Indian Ocean. We also note that over the broad Pacific region, NASA GISS LOTI provides a stronger interhemispheric symmetry

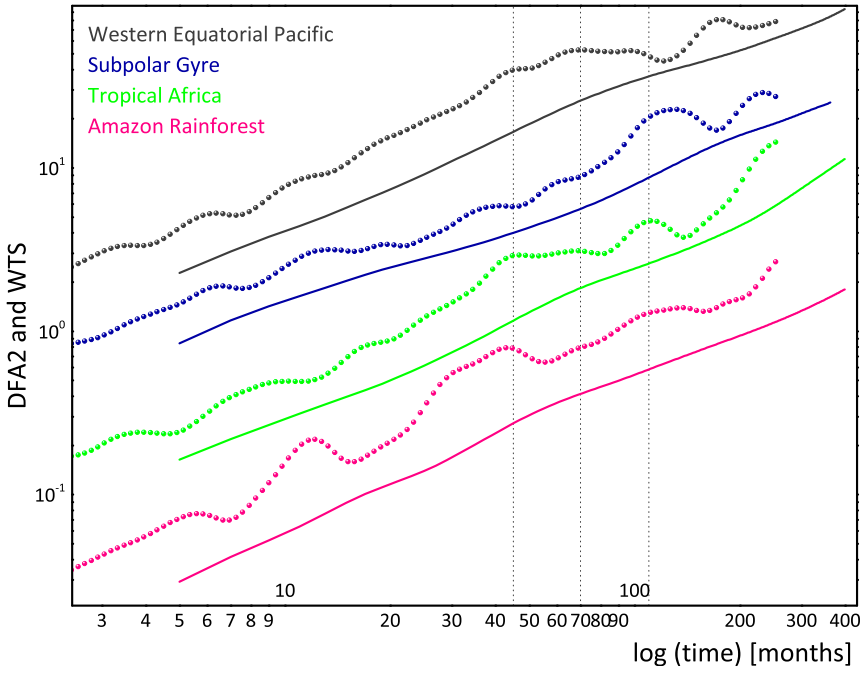

FIG. 6. Examples of the calculated DFA2ff (solid lines) and WTS (filled circles) functions for the grid points in the HadCRUT4 dataset that have scaling exponents $\alpha > 1$. Vertical lines at $t = 45$, 70, and 110 months are given as visual guides.

in the LTP values, compared to HadCRUT4, and a clearer identification of the extratropical gyres in both hemispheres. These differences are likely to yield different representations in both datasets of the Pacific decadal oscillation, centered in the northern basin, as well as of the interdecadal Pacific oscillation, straddling the northern and southern basins. In what follows, we will try to evaluate the dissimilarity in dataset construction methodologies as a source for the obtained dataset dissimilarity in regional scaling.

c. *Understanding differences in scaling between HadCRUT4 and NASA GISS LOTI*

1) LAND: EFFECTS OF THE 1200-KM RULE

Here, HadCRUT4–NASA GISS LOTI differences in values of scaling over the land are assessed, accounting for the different approaches employed to solve the problem of incomplete spatial coverage in their construction. HadCRUT4 does not employ any form of spatial infilling, and as a result, gridbox anomalies can readily be traced back to observational records (Morice et al. 2012). NASA GISS LOTI instead interpolates among station measurements and extrapolates anomalies as far as 1200 km into regions without measurement stations (Hansen et al. 2010). To probe whether the spatial infilling that is employed in the construction of the NASA GISS dataset determines the observed difference in scaling over land between NASA GISS and HadCRUT4, we compared the average DFA2ff and WTS of the raw adjusted station records that contribute to a HadCRUT4 grid point, with the DFA2–WTS HadCRUT4 (adjusted) results and the NASA GISS LOTI DFA2–WTS results within the corresponding grid point. We repeated this procedure for several sparsely filled (in terms of number of recording stations) and several densely populated grid points. Examples of our findings are given in Fig. 8. Our results show that in sparsely filled grid cells, the procedure of spatial interpolation of station data, which is the only data processing performed in the HadCRUT4 dataset, lowers the scaling exponent α due to the modulation of the interannual and multidecadal variability and the flattening of noise at scales higher than annual. This finding is not universal for all spatially averaged HadCRUT4 data; it depends on the relative influence of the high LTP records present within the considered grid box. In NASA GISS LOTI, the additional procedure of spatial infilling within a 1200-km radius from the selected grid point increases this effect (i.e., it further decreases the value of α; see left panels in Fig. 8). Moreover, in the case presented in Fig. 8, the surrounding land grid points have significantly different scaling exponents, so that the process of extrapolation as far as 1200 km integrates spurious

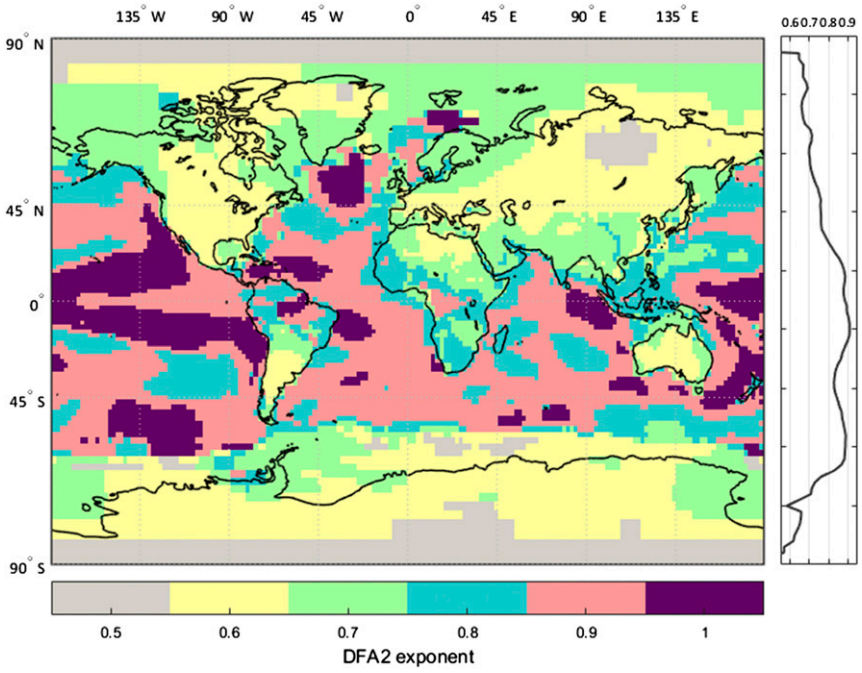

FIG. 7. (left) DFA2 exponents α calculated for all available gridpoint time series of temperature anomalies in the NASA GISS LOTI dataset. Values of $0 < \alpha < 0.45$ belong to grid boxes with missing data. (right) Latitudinal averages of α, calculated along the 90 latitude rows of the GISS dataset (y-axis grid lines are inserted as visual guides).

correlations that are entirely location related (i.e., dependent on the scaling of the nearest-neighbor grid cells). For this reason, changes in the values of α over land introduced by the 1200-km rule in sparsely filled grid boxes cannot be viewed or corrected as for the systematic bias. Finally, the observed discrepancy between HadCRUT4 and NASA GISS LOTI scaling does not appear at grid points sufficiently populated

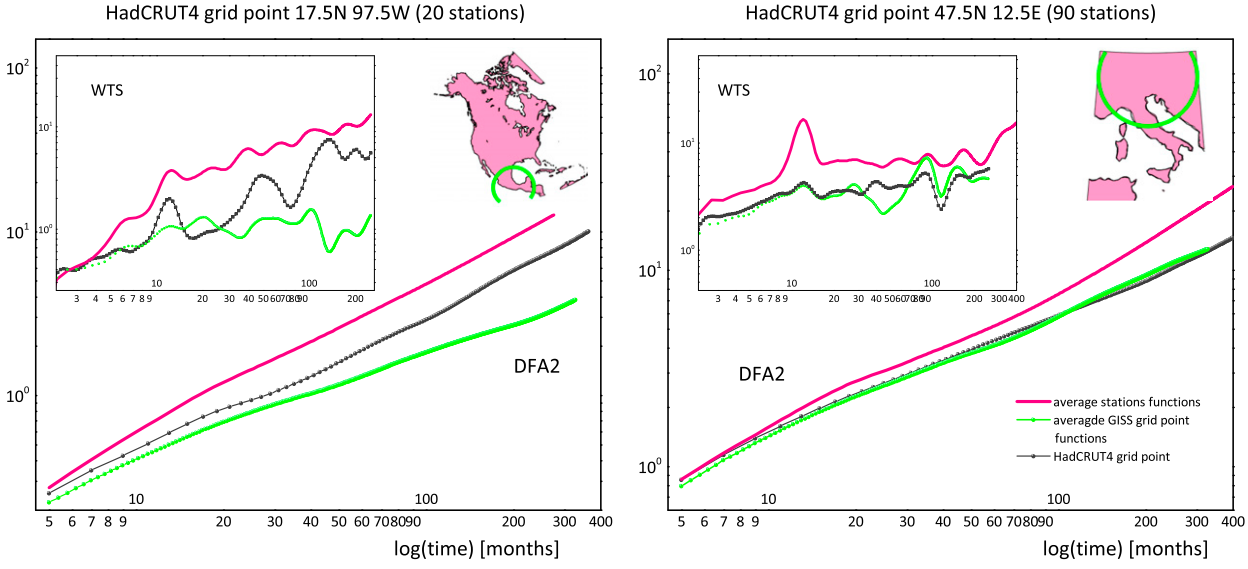

FIG. 8. An example of the effect of a spatial infilling procedure on DFA2–WTS calculations for (left) sparsely infilled and (right) sufficiently populated HadCRUT4 grid points. Depicted are average DFA2ff of the station records that compose grid points (pink solid line), the average DFA2ff of the four NASA GISS LOTI grid points encompassed by the grid point analyzed (green filled circles), and the DFA2 HadCRUT4 results (gray filled circles), with the corresponding WTS given in the figure insets.

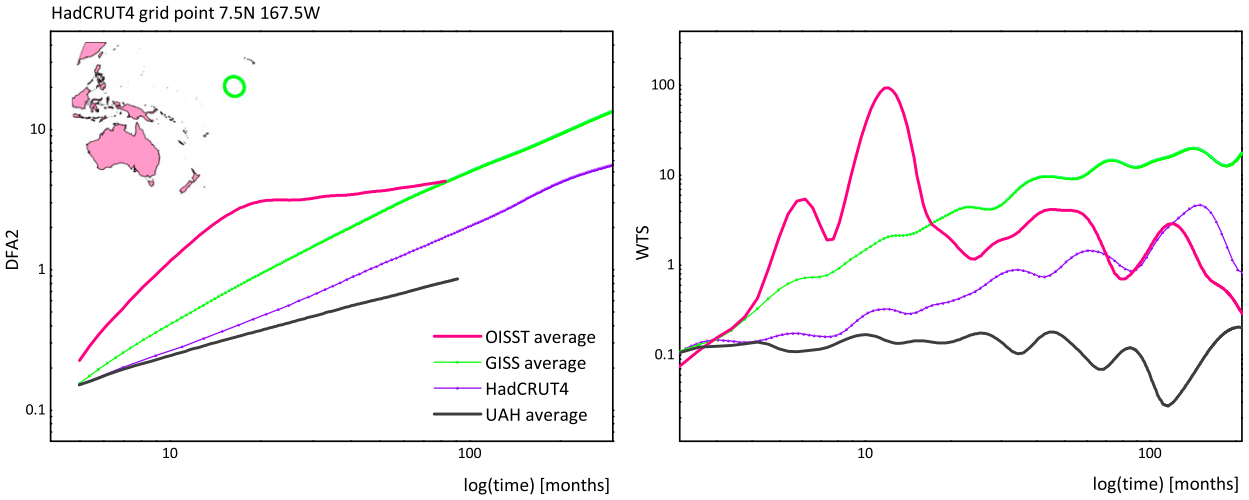

FIG. 9. Comparison of DFA2–WTS HadCRUT4 gridpoint scaling results (violet-filled circles) with the matching average of four (within the same HadCRUT4 grid point) NASA GISS results (green-filled circles), the average of 25 OISSTv2 results (pink solid line), and the average of four UAH satellite temperature results for TLT scaling (gray solid line). The results are given for the HadCRUT4 grid box centered at 7.5°N, 167.5°W.

with recording stations (see example in the right panels of Fig. 8).

2) OCEAN: EFFECTS OF INCLUSION OF SATELLITE DATA

NASA GISS LOTI constructs ocean data (Hansen et al. 2010) as an integration of the Met Office Hadley Centre analysis of SSTs (HadISST1; the sole basis of HadCRUT4 ocean data; Rayner et al. 2003) for the 1880–1981 period, where measurements are ship based, and satellite SST measurements (OISSTv2; Reynolds et al. 2007) from 1982 to the present. Satellite measurements in the NASA GISS dataset are additionally calibrated with the help of ship and buoy data (Hansen et al. 2010). To understand how this methodological difference affects scaling over ocean regions in both datasets, we calculated and compared DFA2ff and WTS of several HadCRUT4 marine grid points with the matching average (within the same HadCRUT4 grid cell) NASA GISS LOTI, average OISSTv2, and average UAH satellite temperature for the lower troposphere (TLT) scaling. An example of the obtained findings is given in Fig. 9, showing the TLT UAH data scale as white noise (with $\alpha \approx 0.5$ and flat $\beta \approx 0$ WTS). Thus, it seems that the optimization procedure employed in the construction of OISSTv2 raises the DFA2–WTS slopes of the NASA GISS data, leading to the higher NASA GISS LOTI scaling. From the WTS given in Fig. 9, it is apparent that this effect is most prominent in the range of scales of up to 1 year, which is very likely the result of the superimposed seasonality on the marine satellite record. This result was robust for all the grid points that we probed.

4. Discussion and conclusions

We used detrended fluctuation analysis of second-order (DFA2) and wavelet-based spectral (WTS) analysis to investigate and quantify the global pattern of scaling in major datasets of observed near-surface air temperature anomalies and to better understand cyclic behavior as a possible underlying cause of the observed long-term scaling behavior. Both methods allow us to overcome problems related to nonlinearity and partially nonstationarity of natural data series. We focused our analysis on two prominent sources of global temperature data, namely, the Met Office HadCRUT4 and the NASA GISS LOTI gridded historical records. Our approach allowed us to characterize the global pattern of temperature scaling and to investigate the relevance and the extent of possible influences of real or artificial (i.e., originated by data processing) cycles upon global scaling. In particular, we investigated how DFA2ff and WTS can be affected by data processing compensating for the issue of inhomogeneity of data linked to the scarcity of records or to the changes of data-recording practices. Finally, we studied the possible structural sources of dissimilarities in global pattern of scaling that we found to exist between the HadCRUT4 and NASA GISS LOTI datasets.

We found that the global temperature pattern is likely long-range autocorrelated, except for polar and parts of

subpolar regions, where data inhomogeneity is substantial. We confirmed the existence of a land–ocean contrast in persistence (Bunde and Havlin 2002; Fraedrich and Blender 2003), with marine data showing an appreciably more pronounced long-range persistence than land data. Four prominent cyclic influences, or characteristic times of underlying processes, emerged in the time range of analysis of our data. They appear at periods of 12, ~40, 72, and 110 months. The first two cycles that we found in our data can be attributed to the seasonal cycle and probably to the influence of the leading ENSO eigenmode (Penland and Matrosova 2006; Compo and Sardeshmukh 2010) on sea surface and land temperatures. The other two characteristic times are difficult to attribute to any individual or canonical source of climate variability. We refer to research showing that the period of approximately 6 years can be related to the variance of ENSO indices such as Niño-3.4 SSTs (Penland and Matrosova 2006) or to the first harmonics of decadal variabilities (Zanchettin et al. 2013), while the near-decadal period of 110 months can emerge as a response to nonperiodic strong events of volcanic eruptions (Rypdal 2012; Lovejoy and Varotsos 2016) or as a reflection of decadal climate variability originated either by internal processes (Liu 2012) or forced by external natural factors (Zanchettin 2017). A systematic assessment of the observational records that will explore the universality of appearance of the range of cycles obtained here remains a task for future research. Understanding of universality and of the nature of these irregular structures, be they periodic or nonperiodic phenomena or even significant singular events (Mallat and Hwang 1992; Zanchettin 2017), may be used as a tool to objectively differentiate between climate scaling regimes (Stratimirović et al. 2018) or as an additional source of information in climate modeling efforts (Lima and Lall 2010).

We found that the spatial average of scaling of the global gridded temperatures is significantly lower than the scaling of the spatially averaged global temperature time series and argued that this is an effect of the disproportionate influence of the high LTP series, particularly those in the midlatitudes, on regional, hemispheric, and global averages. We showed that the global temperature scaling is in this way dominated by the scaling of the Southern Hemisphere, which in turn is possibly significantly determined by the scaling in the tropics. This effect may explain why our values of DFA2 exponents averaged along parallels, particularly along the midlatitudes, differ from the corresponding averages calculated for the global coupled general circulation models by Rybski et al. (2008). Finally, these observations may indicate that the spatial resolution of global temperature products can affect their local (individual grid cells) and global scaling behaviors and that the spatial scaling may be important for understanding the dynamics underlying the observed climate variability. There is probably a need in climatically diverse regions for a more detailed sampling of the different areas (in both datasets) in order to account for their different scaling regimes in the regional estimate and to accurately determine regional dynamics. Sea ice dynamics seem to have a strong effect on scaling, as demonstrated by the sharp edges in the DFA2 exponents consistently detected in NASA GISS LOTI and HadCRUT4 between areas affected and not affected by sea ice. Whether the low persistence observed in the sea ice regions originates from the strong seasonal cycle of sea ice, rather than from other processes of the coupled ocean–atmosphere–sea ice system, remains to be determined.

Our results unraveled the nonuniformity of scaling within ocean or land data and the pronounced differences of such nonuniformity in the two datasets. Our findings suggest that the observed nonuniformity of scaling can reflect a number of different natural (Fraedrich and Blender 2003), as well as methodological, causes, whose individual contribution is difficult to disentangle. We found that for the still-predominant part of the analyzed datasets affected by a large percentage of missing values, the real values of the scaling exponents are likely higher than those calculated. This result is in accordance with assessments of artificial data with similar properties (Rust et al. 2008). We found instances of amplification of cyclic influence or even introduction of new cycles, sometimes coupled with the reduction of noise, in both datasets and due to the homogenization and optimization of the raw (unadjusted) temperature time series; these effects are probably more pronounced in cases of corrections due to the actual data loss (Chen et al. 2002; Ma et al. 2010). Since there is no apparent universal solution to this problem, we avoid conclusively asserting the exact nature of the dynamics underlying the temperature time series for such locations.

We also assessed structural uncertainties that arise from methodological choices made in the two temperature analysis products. We showed instances where spurious scaling is introduced in the NASA GISS dataset through spatial infilling procedure, or where reinforcement of the annual cycle is introduced due to the optimization of integrated satellite records. This highlights once more the need to consult in detail how data are prepared before assessing climate dynamics based on data analysis (von Storch et al. 2012). Nevertheless, keeping in mind the stochastic nature of climate (Hasselmann 1976; Franzke et al. 2012; Watkins 2017)

and the current lack of an effective model capable of capturing long-range interactions between large numbers of interacting parts that would mimic LTP as an output from various climate systems (Ludescher et al. 2017), the observed global temperature pattern of scaling can serve as a nontrivial test (Monetti et al. 2003) for dynamic properties of current climate models.

Our results do not settle the debate about nature and origins of scaling properties of temperature or of the observed natural nonuniformity of scaling (Levine and McPhaden 2016; Markonis and Koutsoyiannis 2013; Bunde and Lennartz 2012; Rypdal 2012; Fraedrich et al. 2004; Stanley 1999; Press 1978). Instead, they point to the heterogeneity of scaling as an important area for further investigation in this context. This seems to be crucial for progress in our understanding of the critical problem of detection and attribution of trends and other climate change evidence (Crok et al. 2014; Zanchettin 2017). Specifically, if we assume that the observed temperature evolution, similar for both datasets (IPCC 2013, their Fig. 2.20), is a realization of a long-term autocorrelated process, then the appropriate statistical approaches and underlying theories must be applied to the detection problem. Current analytical approaches and numerical estimations (Lennartz and Bunde 2009, 2011) indicate the DFA2 scaling exponent α, along with the observed linear trend and the standard deviation around the data regression line, to be an important quantity to estimate anthropogenic trends. The heterogeneous scaling of global temperature reported in our study, and especially the presented evidence of weakly correlated or even random (with $\alpha \approx 0.5$) fluctuations in gridded temperature data, fosters further investigation.

Acknowledgments. Suzana Blesić would like to thank Prof. Armin Bunde for the invaluable introductory advice on and insights into the analysis of time series of climate data. Her work received funding from the European Union's Horizon 2020 Research and Innovation Programme under the Marie Skłodowska-Curie Grant Agreement 701785. We thank Djordje Stratimirović and Darko Sarvan for very useful discussions. Finally, we thank the anonymous reviewers for stimulating comments and particularly for pointing out the critical issue of scaling of spatial averages.

REFERENCES

Alexandersson, H., 1986: A homogeneity test applied to precipitation data. *Int. J. Climatol.*, **6**, 661–675, https://doi.org/10.1002/joc.3370060607.

Alvarez-Ramirez, J., J. Alvarez, L. Dagdug, E. Rodriguez, and J. C. Echeverria, 2008a: Long-term memory dynamics of continental and oceanic monthly temperatures in the recent 125 years. *Physica A*, **387**, 3629–3640, https://doi.org/10.1016/j.physa.2008.02.051.

——, J. C. Echeverria, and E. Rodriguez, 2008b: Performance of a high-dimensional *R*/*S* method for Hurst exponent estimation. *Physica A*, **387**, 6452–6462, https://doi.org/10.1016/j.physa.2008.08.014.

Ashkenazy, Y., D. R. Baker, H. Gildor, and S. Havlin, 2003: Nonlinearity and multifractality of climate change in the past 420,000 years. *Geophys. Res. Lett.*, **30**, 2146, https://doi.org/10.1029/2003GL018099.

Banzon, V., T. M. Smith, T. M. Chin, C. Liu, and W. Hankins, 2016: A long-term record of blended satellite and in situ sea-surface temperature for climate monitoring, modeling and environmental studies. *Earth Syst. Sci. Data*, **8**, 165–176, https://doi.org/10.5194/essd-8-165-2016.

Bashan, A., R. Bartsch, J. W. Kantelhardt, and S. Havlin, 2008: Comparison of detrending methods for fluctuation analysis. *Physica A*, **387**, 5080–5090, https://doi.org/10.1016/j.physa.2008.04.023.

Berezin, Y., A. Gozolchiani, O. Guez, and S. Havlin, 2012: Stability of climate networks with time. *Sci. Rep.*, **2**, 666, https://doi.org/10.1038/srep00666.

Blesić, S., S. Milošević, D. Stratimirović, and M. Ljubisavljević, 1999: Detrended fluctuation analysis of time series of a firing fusimotor neuron. *Physica A*, **268**, 275–282, https://doi.org/10.1016/S0378-4371(99)00110-7.

——, ——, ——, and ——, 2003: Detecting long-range correlations in time series of neuronal discharges. *Physica A*, **330**, 391–399, https://doi.org/10.1016/j.physa.2003.09.002.

Bračič, M., and A. Stefanovska, 1998: Wavelet-based analysis of human blood-flow dynamics. *Bull. Math. Biol.*, **60**, 919–935, https://doi.org/10.1006/bulm.1998.0047.

Buldyrev, S. V., A. L. Goldberger, S. Havlin, R. N. Mantegna, M. E. Matsa, C. K. Peng, M. Simons, and H. E. Stanley, 1995: Long-range correlation properties of coding and noncoding DNA sequences: GenBank analysis. *Phys. Rev. E*, **51**, 5084–5091.

Bunde, A., and S. Havlin, 2002: Power-law persistence in the atmosphere and in the oceans. *Physica A*, **314**, 15–24, https://doi.org/10.1016/S0378-4371(02)01050-6.

——, and S. Lennartz, 2012: Long-term correlations in earth sciences. *Acta Geophysica*, **60**, 562–588, https://doi.org/10.2478/s11600-012-0034-8.

——, J. F. Eichner, S. Havlin, E. Koscielny-Bunde, H. J. Schellnhuber, and D. Vyushin, 2004: Comment on "Scaling of atmosphere and ocean temperature correlations in observations and climate models." *Phys. Rev. Lett.*, **92**, 039801, https://doi.org/10.1103/PhysRevLett.92.039801.

——, M. I. Bogachev, and S. Lennartz, 2013a: Precipitation and river flow: Long-term memory and predictability of extreme events. *Extreme Events and Natural Hazards: The Complexity Perspective*, *Geophys. Monogr.*, Vol. 196, Amer. Geophys. Union, 139–152, https://doi.org/10.1029/2011GM001112.

——, U. Büntgen, J. Ludescher, J. Luterbacher, and H. Von Storch, 2013b: Is there memory in precipitation? *Nat. Climate Change*, **3**, 174–175, https://doi.org/10.1038/nclimate1830.

Carvalho, L. M., A. A. Tsonis, C. Jones, H. R. Rocha, and P. S. Polito, 2007: Anti-persistence in the global temperature anomaly field. *Nonlinear Processes Geophys.*, **14**, 723–733, https://doi.org/10.5194/npg-14-723-2007.

Chen, Z., P. C. Ivanov, K. Hu, and H. E. Stanley, 2002: Effect of nonstationarities on detrended fluctuation analysis. *Phys. Rev. E*, **65**, 041107, https://doi.org/10.1103/PhysRevE.65.041107.

——, K. Hu, P. Carpena, P. Bernaola-Galvan, H. E. Stanley, and P. C. Ivanov, 2005: Effect of nonlinear filters on detrended

fluctuation analysis. *Phys. Rev. E*, **71**, 011104, https://doi.org/10.1103/PhysRevE.71.011104.

Christy, J. R., and R. W. Spencer, 2017: Global temperature report archives. Earth System Science Center, University of Alabama in Huntsville, https://www.nsstc.uah.edu/climate/archives.html.

——, ——, W. B. Norris, W. D. Braswell, and D. E. Parker, 2003: Error estimates of version 5.0 of MSU–AMSU bulk atmospheric temperatures. *J. Atmos. Oceanic Technol.*, **20**, 613–629, https://doi.org/10.1175/1520-0426(2003)20<613:EEOVOM>2.0.CO;2.

Compo, G. P., and P. D. Sardeshmukh, 2010: Removing ENSO-related variations from the climate record. *J. Climate*, **23**, 1957–1978, https://doi.org/10.1175/2009JCLI2735.1.

Crok, M., B. Verheggen, R. van Dorland, and B. Strengers, 2014: Extended summary of the climate dialogue on long term persistence. ClimateDialogue.org, 21 pp., https://www.mwenb.nl/wp-content/uploads/2014/04/Climatedialogue.org-extended-summary-long-term-persistence.pdf.

CRUTEM4 Team, 2017: Met Office Hadley Centre observations datasets: CRUTEM4 data download. Met Office, accessed 5 June 2018, https://www.metoffice.gov.uk/hadobs/crutem4/data/download.html.

Eichner, J. F., E. Koscielny-Bunde, A. Bunde, S. Havlin, and H. J. Schellnhuber, 2003: Power-law persistence and trends in the atmosphere: A detailed study of long temperature records. *Phys. Rev. E*, **68**, 046133, https://doi.org/10.1103/PhysRevE.68.046133.

Fraedrich, K., and R. Blender, 2003: Scaling of atmosphere and ocean temperature correlations in observations and climate models. *Phys. Rev. Lett.*, **90**, 108501, https://doi.org/10.1103/PhysRevLett.90.108501.

——, and ——, 2004: Fraedrich and Blender reply. *Phys. Rev. Lett.*, **92**, 039802, https://doi.org/10.1103/PhysRevLett.92.039802.

——, U. Luksch, and R. Blender, 2004: 1/*f* model for long-time memory of the ocean surface temperature. *Phys. Rev. E*, **70**, 037301, https://doi.org/10.1103/PhysRevE.70.037301.

Franzke, C. L. E., T. Graves, N. W. Watkins, R. B. Gramacy, and C. Hughes, 2012: Robustness of estimators of long-range dependence and self-similarity under non-Gaussianity. *Philos. Trans. Roy. Soc.*, **370A**, 1250–1267, https://doi.org/10.1098/rsta.2011.0349.

——, T. J. O'Kane, J. Berner, P. D. Williams, and V. Lucarini, 2015: Stochastic climate theory and modeling. *Wiley Interdiscip. Rev.: Climate Change*, **6**, 63–78, https://doi.org/10.1002/wcc.318.

Freeman, E., and Coauthors, 2017: ICOADS release 3.0: A major update to the historical marine climate record. *Int. J. Climatol.*, **37**, 2211–2232, https://doi.org/10.1002/joc.4775.

GHCN Team, 2017: Global Historical Climatology Network (GHCN). NOAA/NCEI, accessed 5 June 2018, https://www.ncdc.noaa.gov/data-access/land-based-station-data/land-based-datasets/global-historical-climatology-network-ghcn.

GISTEMP Team, 2017: GISS Surface Temperature Analysis (GISTEMP). NASA/GISS, accessed 18 September 2017, https://data.giss.nasa.gov/gistemp.

Goupillaud, P., A. Grossmann, and J. Morlet, 1984: Cycle-octave and related transforms in seismic signal analysis. *Geoexploration*, **23**, 85–102, https://doi.org/10.1016/0016-7142(84)90025-5.

Govindan, R. B., A. Bunde, and S. Havlin, 2003: Volatility in atmospheric temperature variability. *Physica A*, **318**, 529–536, https://doi.org/10.1016/S0378-4371(02)01552-2.

Graf, H. F., and D. Zanchettin, 2012: Central Pacific El Niño, the "subtropical bridge," and Eurasian climate. *J. Geophys. Res.*, **117**, D01102, https://doi.org/10.1029/2011JD016493.

Grossmann, A., and J. Morlet, 1984: Decomposition of Hardy functions into square integrable wavelets of constant shape. *SIAM J. Math. Anal.*, **15**, 723–736, https://doi.org/10.1137/0515056.

Hansen, J., R. Ruedy, M. Sato, and K. Lo, 2010: Global surface temperature change. *Rev. Geophys.*, **48**, RG4004, https://doi.org/10.1029/2010RG000345.

Hasselmann, K., 1976: Stochastic climate models. Part I: Theory. *Tellus*, **28**, 473–485, https://doi.org/10.3402/tellusa.v28i6.11316.

Höll, M., and H. Kantz, 2015: The relationship between the detrended fluctuation analysis and the autocorrelation function of a signal. *Eur. Phys. J. B*, **88**, 327, https://doi.org/10.1140/epjb/e2015-60721-1.

——, ——, and Y. Zhou, 2016: Detrended fluctuation analysis and the difference between external drifts and intrinsic diffusion-like nonstationarity. *Phys. Rev. E*, **94**, 042201, https://doi.org/10.1103/PhysRevE.94.042201.

Hu, K., P. C. Ivanov, Z. Chen, P. Carpena, and H. E. Stanley, 2001: Effect of trends on detrended fluctuation analysis. *Phys. Rev. E*, **64**, 011114, https://doi.org/10.1103/PhysRevE.64.011114.

Huang, B., and Coauthors, 2015: Extended Reconstructed Sea Surface Temperature version 4 (ERSST.v4). Part I: Upgrades and intercomparisons. *J. Climate*, **28**, 911–930, https://doi.org/10.1175/JCLI-D-14-00006.1.

——, and Coauthors, 2016: Further exploring and quantifying uncertainties for Extended Reconstructed Sea Surface Temperature (ERSST) version 4 (v4). *J. Climate*, **29**, 3119–3142, https://doi.org/10.1175/JCLI-D-15-0430.1.

Hurst, H. E., 1951: Long-term storage capacity of reservoirs. *Trans. ASCE*, **116**, 770–799.

IPCC, 2013: *Climate Change 2013: The Physical Science Basis*. Cambridge University Press, 1535 pp., https://doi.org/10.1017/CBO9781107415324.

Jones, P. D., D. H. Lister, T. J. Osborn, C. Harpham, M. Salmon, and C. P. Morice, 2012: Hemispheric and large-scale land-surface air temperature variations: An extensive revision and an update to 2010. *J. Geophys. Res.*, **117**, D05127, https://doi.org/10.1029/2011JD017139.

Kantelhardt, J. W., E. Koscielny-Bunde, H. H. Rego, S. Havlin, and A. Bunde, 2001: Detecting long-range correlations with detrended fluctuation analysis. *Physica A*, **295**, 441–454, https://doi.org/10.1016/S0378-4371(01)00144-3.

——, ——, D. Rybski, P. Braun, A. Bunde, and S. Havlin, 2006: Long-term persistence and multifractality of precipitation and river runoff records. *J. Geophys. Res.*, **111**, D01106, https://doi.org/10.1029/2005JD005881.

Karl, T. R., R. G. Quayle, and P. Ya. Groisman, 1993: Detecting climate variations and change: New challenges for observing and data management systems. *J. Climate*, **6**, 1481–1494, https://doi.org/10.1175/1520-0442(1993)006<1481:DCVACN>2.0.CO;2.

KNMI Team, 2017: KNMI Climate Explorer: Starting point. KNMI, accessed 5 June 2018, https://climexp.knmi.nl/start.cgi.

Koscielny-Bunde, E., J. W. Kantelhardt, P. Braun, A. Bunde, and S. Havlin, 2006: Long-term persistence and multifractality of river runoff records: Detrended fluctuation studies. *J. Hydrol.*, **322**, 120–137, https://doi.org/10.1016/j.jhydrol.2005.03.004.

Koutsoyiannis, D., 2003: Climate change, the Hurst phenomenon, and hydrological statistics. *Hydrol. Sci. J.*, **48**, 3–24, https://doi.org/10.1623/hysj.48.1.3.43481.

Lawrimore, J. H., M. J. Menne, B. E. Gleason, C. N. Williams, D. B. Wuertz, R. S. Vose, and J. Rennie, 2011: An overview of the Global Historical Climatology Network monthly mean temperature data set, version 3. *J. Geophys. Res.*, **116**, D19121, https://doi.org/10.1029/2011JD016187.

Lennartz, S., and A. Bunde, 2009: Trend evaluation in records with long-term memory: Application to global warming. *Geophys. Res. Lett.*, **36**, L16706, https://doi.org/10.1029/2009GL039516.

——, and ——, 2011: Distribution of natural trends in long-term correlated records: A scaling approach. *Phys. Rev. E*, **84**, 021129, https://doi.org/10.1103/PhysRevE.84.021129.

Levine, A. F., and M. J. McPhaden, 2016: How the July 2014 easterly wind burst gave the 2015–2016 El Niño a head start. *Geophys. Res. Lett.*, **43**, 6503–6510, https://doi.org/10.1002/2016GL069204.

Lima, C. H., and U. Lall, 2010: Spatial scaling in a changing climate: A hierarchical Bayesian model for non-stationary multi-site annual maximum and monthly streamflow. *J. Hydrol.*, **383**, 307–318, https://doi.org/10.1016/j.jhydrol.2009.12.045.

Liu, Z., 2012: Dynamics of interdecadal climate variability: A historical perspective. *J. Climate*, **25**, 1963–1995, https://doi.org/10.1175/2011JCLI3980.1.

Livina, V. N., Y. Ashkenazy, A. Bunde, and S. Havlin, 2011: Seasonality effects on nonlinear properties of hydrometeorological records. *In Extremis: Disruptive Events and Trends in Climate and Hydrology*, J. Kropp and H.-J. Schellnhuber, Eds., Springer, 266–284, https://doi.org/10.1007/978-3-642-14863-7_13.

Lovejoy, S., and D. Schertzer, 2013: Low-frequency weather and the emergence of the climate. *Extreme Events and Natural Hazards: The Complexity Perspective*, *Geophys. Monogr.*, Vol. 196, Amer. Geophys. Union, 231–254, https://doi.org/10.1029/2011GM001087.

——, and C. Varotsos, 2016: Scaling regimes and linear/nonlinear responses of last millennium climate to volcanic and solar forcings. *Earth Syst. Dyn.*, **7**, 133–150, https://doi.org/10.5194/esd-7-133-2016.

Ludescher, J., M. I. Bogachev, J. W. Kantelhardt, A. Y. Schumann, and A. Bunde, 2011: On spurious and corrupted multifractality: The effects of additive noise, short-term memory and periodic trends. *Physica A*, **390**, 2480–2490, https://doi.org/10.1016/j.physa.2011.03.008.

——, A. Bunde, C. L. Franzke, and H. J. Schellnhuber, 2016: Long-term persistence enhances uncertainty about anthropogenic warming of Antarctica. *Climate Dyn.*, **46**, 263–271, https://doi.org/10.1007/s00382-015-2582-5.

——, ——, and H. J. Schellnhuber, 2017: Statistical significance of seasonal warming/cooling trends. *Proc. Natl. Acad. Sci. USA*, **114**, E2998–E3003, https://doi.org/10.1073/pnas.1700838114.

Luo, M., Y. Leung, Y. Zhou, and W. Zhang, 2015: Scaling behaviors of global sea surface temperature. *J. Climate*, **28**, 3122–3132, https://doi.org/10.1175/JCLI-D-13-00743.1.

Ma, Q. D., R. P. Bartsch, P. Bernaola-Galván, M. Yoneyama, and P. C. Ivanov, 2010: Effect of extreme data loss on long-range correlated and anticorrelated signals quantified by detrended fluctuation analysis. *Phys. Rev. E*, **81**, 031101, https://doi.org/10.1103/PhysRevE.81.031101.

Mallat, S., and W. L. Hwang, 1992: Singularity detection and processing with wavelets. *IEEE Trans. Inf. Theory*, **38**, 617–643, https://doi.org/10.1109/18.119727.

Mandelbrot, B. B., 2001: Harold Edwin Hurst. *Statisticians of the Centuries*, C. C. Heyde et al., Eds., Springer, 335–338, https://doi.org/10.1007/978-1-4613-0179-0_72.

——, and J. R. Wallis, 1968: Noah, Joseph, and operational hydrology. *Water Resour. Res.*, **4**, 909–918, https://doi.org/10.1029/WR004i005p00909.

——, and ——, 1969: Robustness of the rescaled range R/S in the measurement of noncyclic long run statistical dependence. *Water Resour. Res.*, **5**, 967–988, https://doi.org/10.1029/WR005i005p00967.

Markonis, Y., and D. Koutsoyiannis, 2013: Climatic variability over time scales spanning nine orders of magnitude: Connecting Milankovitch cycles with Hurst–Kolmogorov dynamics. *Surv. Geophys.*, **34**, 181–207, https://doi.org/10.1007/s10712-012-9208-9.

Menne, M. J., and C. N. Williams, 2009: Homogenization of temperature series via pairwise comparisons. *J. Climate*, **22**, 1700–1717, https://doi.org/10.1175/2008JCLI2263.1.

Met Office Hadley Centre, 2010: Met Office Hadley Centre observations datasets. Met Office, accessed 5 June 2018, http://hadobs.metoffice.com/hadcrut3/diagnostics/comparison.html.

Milošević, S., S. Blesić, and D. Stratimirović, 2002: Beneficial randomness of signals in a neuronal circuit. *Physica A*, **314**, 43–52, https://doi.org/10.1016/S0378-4371(02)01184-6.

Monetti, R. A., S. Havlin, and A. Bunde, 2003: Long-term persistence in the sea surface temperature fluctuations. *Physica A*, **320**, 581–589, https://doi.org/10.1016/S0378-4371(02)01662-X.

Morice, C. P., J. J. Kennedy, N. A. Rayner, and P. D. Jones, 2012: Quantifying uncertainties in global and regional temperature change using an ensemble of observational estimates: The HadCRUT4 data set. *J. Geophys. Res.*, **117**, D08101, https://doi.org/10.1029/2011JD017187.

Morlet, J., 1983: Sampling theory and wave propagation. Issues in Acoustic Signal—Image Processing and Recognition, C. H. Chen, Ed., NATO ASI Series, Vol. 1, Springer, 233–261, https://doi.org/10.1007/978-3-642-82002-1_12.

OISST Team, 2017: Index of /data/sea-surface-temperature-optimum-interpolation/access. NOAA/NCEI, accessed 5 June 2018, https://www.ncei.noaa.gov/data/sea-surface-temperature-optimum-interpolation/access/.

Osborn, T. J., and P. D. Jones, 2014: The CRUTEM4 land-surface air temperature data set: Construction, previous versions and dissemination via Google Earth. *Earth Syst. Sci. Data*, **6**, 61–68, https://doi.org/10.5194/essd-6-61-2014.

Peng, C. K., S. V. Buldyrev, A. L. Goldberger, S. Havlin, M. Simons, and H. E. Stanley, 1993: Finite-size effects on long-range correlations: Implications for analyzing DNA sequences. *Phys. Rev. E*, **47**, 3730–3733.

——, ——, S. Havlin, M. Simons, H. E. Stanley, and A. L. Goldberger, 1994: Mosaic organization of DNA nucleotides. *Phys. Rev. E*, **49**, 1685–1689.

——, S. Havlin, H. E. Stanley, and A. L. Goldberger, 1995: Quantification of scaling exponents and crossover phenomena in nonstationary heartbeat time series. *Chaos*, **5**, 82, https://doi.org/10.1063/1.166141.

Penland, C., and L. Matrosova, 2006: Studies of El Niño and interdecadal variability in tropical sea surface temperatures using a nonnormal filter. *J. Climate*, **19**, 5796–5815, https://doi.org/10.1175/JCLI3951.1.

Perrier, V., T. Philipovitch, and C. Basdevant, 1995: Wavelet spectra compared to Fourier spectra. *J. Math. Phys.*, **36**, 1506, https://doi.org/10.1063/1.531340.

Peterson, T. C., and Coauthors, 1998: Homogeneity adjustments of in situ atmospheric climate data: A review. *Int. J. Climatol.*, **18**, 1493–1517, https://doi.org/10.1002/(SICI)1097-0088(19981115)18:13<1493::AID-JOC329>3.0.CO;2-T.

Press, W. H., 1978: Flicker noises in astronomy and elsewhere. *Comments Mod. Phys.*, **7**, 103–119.

Rayner, N. A., D. E. Parker, E. B. Horton, C. K. Folland, L. V. Alexander, D. P. Rowell, E. C. Kent, and A. Kaplan, 2003: Global analyses of sea surface temperature, sea ice, and night marine air temperature since the late nineteenth century. *J. Geophys. Res.*, **108**, 4407, https://doi.org/10.1029/2002JD002670.

Reynolds, R. W., N. A. Rayner, T. M. Smith, D. C. Stokes, and W. Wang, 2002: An improved in situ and satellite SST analysis for climate. *J. Climate*, **15**, 1609–1625, https://doi.org/10.1175/1520-0442(2002)015<1609:AIISAS>2.0.CO;2.

——, T. M. Smith, C. Liu, D. B. Chelton, K. S. Casey, and M. G. Schlax, 2007: Daily high-resolution-blended analyses for sea surface temperature. *J. Climate*, **20**, 5473–5496, https://doi.org/10.1175/2007JCLI1824.1.

Rodriguez, E., M. Aguilar-Cornejo, R. Femat, and J. Alvarez-Ramirez, 2014: US stock market efficiency over weekly, monthly, quarterly and yearly time scales. *Physica A*, **413**, 554–564, https://doi.org/10.1016/j.physa.2014.07.036.

Rust, H. W., O. Mestre, and V. K. Venema, 2008: Fewer jumps, less memory: Homogenized temperature records and long memory. *J. Geophys. Res.*, **113**, D19110, https://doi.org/10.1029/2008JD009919.

Rybski, D., A. Bunde, and H. von Storch, 2008: Long-term memory in 1000-year simulated temperature records. *J. Geophys. Res.*, **113**, D02106, https://doi.org/10.1029/2007JD008568.

Rypdal, K., 2012: Global temperature response to radiative forcing: Solar cycle versus volcanic eruptions. *J. Geophys. Res.*, **117**, D06115, https://doi.org/10.1029/2011JD017283.

Sarvan, D., Đ. Stratimirović, S. Blesić, V. Djurdjevic, V. Miljković, and J. Ajtić, 2017: Dynamics of beryllium-7 specific activity in relation to meteorological variables, tropopause height, teleconnection indices and sunspot number. *Physica A*, **469**, 813–823, https://doi.org/10.1016/j.physa.2016.11.040.

Schertzer, D., and S. Lovejoy, 1987: Physical modeling and analysis of rain and clouds by anisotropic scaling multiplicative processes. *J. Geophys. Res.*, **92**, 9693–9714, https://doi.org/10.1029/JD092iD08p09693.

——, and ——, 1990: *Non-Linear Variability in Geophysics: Scaling and Fractals*. Springer, 332 pp.

Smith, T. M., R. W. Reynolds, T. C. Peterson, and J. Lawrimore, 2008: Improvements to NOAA's historical merged land–ocean surface temperature analysis (1880–2006). *J. Climate*, **21**, 2283–2296, https://doi.org/10.1175/2007JCLI2100.1.

Stanley, H. E., 1999: Scaling, universality, and renormalization: Three pillars of modern critical phenomena. *Rev. Mod. Phys.*, **71**, S358, https://doi.org/10.1103/RevModPhys.71.S358.

——, 2000: Exotic statistical physics: Applications to biology, medicine, and economics. *Physica A*, **285**, 1–17, https://doi.org/10.1016/S0378-4371(00)00341-1.

——, 2005: Correlated randomness: Some examples of exotic statistical physics. *Pramana*, 64, 645–660, https://doi.org/10.1007/BF02704574.

Stratimirović, D., S. Milošević, S. Blesić, and M. Ljubisavljević, 2001: Wavelet analysis of discharge dynamics of fusimotor neurons. *Physica A*, **291**, 13–23, https://doi.org/10.1016/S0378-4371(00)00495-7.

——, D. Sarvan, V. Miljković, and S. Blesić, 2018: Analysis of cyclical behavior in time series of stock market returns. *Commun. Nonlinear Sci. Numer. Simul.*, **54**, 21–33, https://doi.org/10.1016/j.cnsns.2017.05.009.

Talkner, P., and R. Weber, 2000: Power spectrum and detrended fluctuation analysis: Application to daily temperatures. *Phys. Rev. E*, **62**, 150–160.

Tamazian, A., J. Ludescher, and A. Bunde, 2015: Significance of trends in long-term correlated records. *Phys. Rev. E*, **91**, 032806, https://doi.org/10.1103/PhysRevE.91.032806.

Torrence, C., and G. P. Compo, 1998: A practical guide to wavelet analysis. *Bull. Amer. Meteor. Soc.*, **79**, 61–78, https://doi.org/10.1175/1520-0477(1998)079<0061:APGTWA>2.0.CO;2.

——, and ——, 2017: A practical guide to wavelet analysis with significance and confidence testing. University of Colorado Boulder, https://github.com/chris-torrence/wavelets.

Tsonis, A. A., and P. J. Roebber, 2004: The architecture of the climate network. *Physica A*, **333**, 497–504, https://doi.org/10.1016/j.physa.2003.10.045.

——, ——, and J. B. Elsner, 1999: Long-range correlations in the extratropical atmospheric circulation: Origins and implications. *J. Climate*, **12**, 1534–1541, https://doi.org/10.1175/1520-0442(1999)012<1534:LRCITE>2.0.CO;2.

——, A. G. Hunt, and J. B. Elsner, 2003: On the relation between ENSO and global climate change. *Meteor. Atmos. Phys.*, **84**, 229–242, https://doi.org/10.1007/s00703-003-0001-7.

Varotsos, C. A., C. L. Franzke, M. N. Efstathiou, and A. G. Degermendzhi, 2014: Evidence for two abrupt warming events of SST in the last century. *Theor. Appl. Climatol.*, **116**, 51–60, https://doi.org/10.1007/s00704-013-0935-8.

von Storch, H., A. Bunde, and N. Stehr, 2012: The physical sciences and climate politics. *The Oxford Handbook of Climate Change and Society*, J. S. Dryzek, R. B. Norgaard, and D. Schlosberg, Eds., Oxford University Press, 3–8.

Watkins, N. W., 2017: Fractional stochastic models for heavy tailed, and long-range dependent, fluctuations in physical systems. *Nonlinear and Stochastic Climate Dynamics*, C. L. E. Franzke and T. J. O'Kane, Eds., Cambridge University Press, 340–368, https://doi.org/10.1017/9781316339251.013.

Xu, L., P. C. Ivanov, K. Hu, Z. Chen, A. Carbone, and H. E. Stanley, 2005: Quantifying signals with power-law correlations: A comparative study of detrended fluctuation analysis and detrended moving average techniques. *Phys. Rev. E*, **71**, 051101, https://doi.org/10.1103/PhysRevE.71.051101.

Zanchettin, D., 2017: Aerosol and solar irradiance effects on decadal climate variability and predictability. *Curr. Climate Change Rep.*, **3**, 150–162, https://doi.org/10.1007/s40641-017-0065-y.

——, A. Rubino, P. Traverso, and M. Tomasino, 2008: Impact of variations in solar activity on hydrological decadal patterns in northern Italy. *J. Geophys. Res.*, **113**, D12102, https://doi.org/10.1029/2007JD009157.

——, ——, D. Matei, O. Bothe, and J. H. Jungclaus, 2013: Multidecadal-to-centennial SST variability in the MPI-ESM simulation ensemble for the last millennium. *Climate Dyn.*, **40**, 1301–1318, https://doi.org/10.1007/s00382-012-1361-9.

Zorita, E., T. F. Stocker, and H. Von Storch, 2008: How unusual is the recent series of warm years? *Geophys. Res. Lett.*, **35**, L24706, https://doi.org/10.1029/2008GL036228.